# Effects of temperature on tidally influenced coastal unconfined aquifers

Thuy T. M. Nguyen[1, 2], Xiayang Yu[2], Li Pu[2], Pei Xin[1,*], Chenming Zhang[1], D. A. Barry[3] and Ling Li[4,*]

[1]School of Civil Engineering, The University of Queensland, Queensland, Australia

[2]State Key Laboratory of Hydrology-Water Resources and Hydraulic Engineering, Hohai University, Nanjing, China

[3]Laboratoire de technologie écologique (ECOL), Institut d'ingénierie de l'environnement (IIE), Faculté de l'environnement naturel, architectural et construit (ENAC), Ecole Polytechnique Fédérale de Lausanne (EPFL), Lausanne, Switzerland

[4]School of Engineering, Westlake University, Hangzhou, China

[*]Corresponding authors: pei.xin@outlook.com; liling@westlake.edu.cn

## Key points

- The upper saline plume expands whereas the saltwater wedge retreats with increasing seawater temperature
- Warmer seawater enhances the submarine groundwater discharge by intensifying the seawater circulation
- Thermal effects intensify with increased tidal amplitude


## Abstract

Aquifer-ocean temperature contrasts are common worldwide. Their effects on flow and salinity distributions in unconfined coastal aquifers are, however, poorly understood. Based on laboratory experiments and numerical simulations, we examined the responses of flow processes in tidally influenced aquifers to aquifer-ocean temperature differences. The extent of seawater intrusion and seawater circulation were found to vary with the aquifer-ocean temperature contrast. Compared with the isothermal case, an increase of up to 40% of the tide-induced seawater circulation rate in the intertidal zone was observed when seawater is warmer than groundwater. In contrast, saltwater circulation in the lower saltwater wedge declines notably no matter whether the seawater is warmer or colder than groundwater. As the seawater temperature rises, the contribution of tide-induced circulation to the overall increase of submarine groundwater discharge becomes more important compared with that of density-driven seawater circulation. Both the upper saline plume and the freshwater discharge zone expand significantly with warmer seawater whereas the lower saltwater wedge contracts.

**Keywords**

Aquifer; Subterranean estuary; Submarine groundwater discharge; Saltwater intrusion; Temperature

## 1. Introduction

As a connection between land and ocean, coastal aquifers serve as a key reactive and mixing zone between terrestrial freshwater and marine seawater. Due to the density contrast between freshwater and seawater, a lower saltwater wedge develops in the aquifer, above which inland fresh groundwater flows prior to discharge to the sea [*Cooper et al.*, 1964; *Smith*, 2004; *Abarca et al.*, 2007; *Werner et al.*, 2013; *Lu et al.*, 2016]. Hydrodynamic dispersion is a major factor underpinning density-driven seawater circulation in the saltwater wedge [*Cooper et al.*, 1964]. Tidal sea level fluctuations induce a distinct seawater circulation cell (termed upper saline plume, USP) in the intertidal zone, with seawater infiltrating the beach surface at the high tide and exiting the aquifer around the low tidal mark (Fig. 1) [*Robinson et al.*, 2007, 2018; *Xin et al.*, 2010; *Kuan et al.*, 2012; *Yu et al.*, 2019a]. Seawater circulates through this cell with much shorter transit times compared to that for a static saltwater wedge. The USP promotes the entry of oxygen and dissolved organic matter to the subsurface, and helps stimulate respiration and denitrification processes [*Robinson et al.*, 2009; *Anwar et al.*, 2014; *Heiss and Michael*, 2014; *Heiss et al.*, 2017]. The mixing zones associated with the USP and saltwater wedge are important reactive zones for biochemical modification of terrestrially derived contaminants before being discharged to the ocean. Tide-induced seawater circulation also contributes significantly to submarine groundwater discharge (SGD) [*Li* *et al.*, 1999; *Robinson et al.*, 2007; *Moore*, 2010]. The freshwater discharge zone is confined between the USP and saltwater wedge [*Kuan et al.*, 2012].

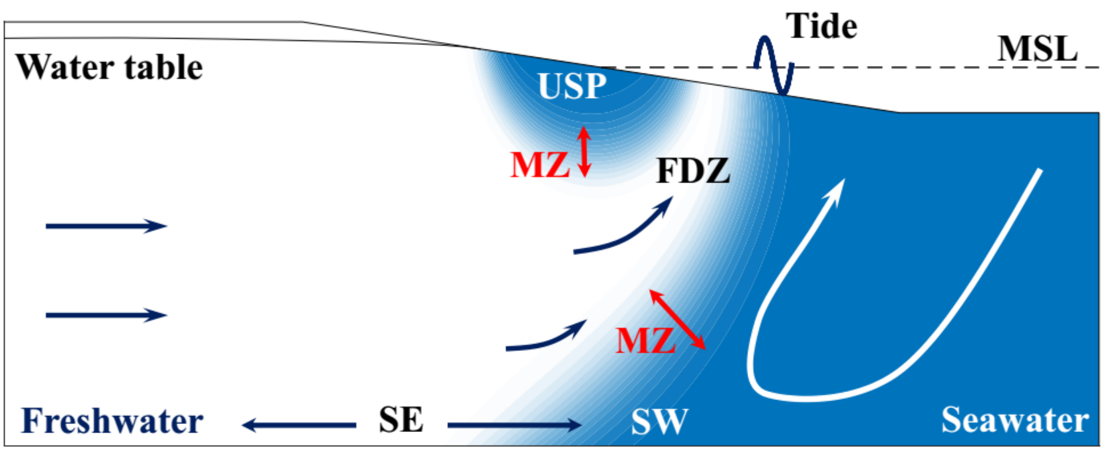


Fig. 1. Conceptual diagram of a typical coastal unconfined aquifer including two seawater circulation zones: An upper saline plume (USP) induced by tides and a density-driven salt wedge (SW). Consequently, upper and lower mixing zones (MZ) associated with these regions are present. The inland freshwater flows across the subterranean estuary (SE) and discharges through a freshwater discharge zone (FDZ) along with the recirculating seawater from both circulation zones. MSL indicates the mean sea level.

Previous studies have reported a close correlation between the USP expansion and biochemical reactivity under various oceanic and terrestrial boundary conditions including tidal amplitude, beach slope, inland freshwater discharge and aquifer properties [*Anwar et al.*, 2014; *Heiss et al.*, 2017; *Kim et al.*, 2017; *Yu et al.*, 2017]. An increase in tidal amplitude pushes the saltwater wedge seaward and creates a larger USP that consequently facilitates biochemical transformation of land-sourced contaminants via the introduction of oxygen and organic matter [*Santos et al.*, 2008; *Charbonnier et al.*, 2013; *Anwar et al.*, 2014]. Whereas, an increased inland freshwater flux inhibits the expansion of the USP and upper mixing zone, and so reduces local biochemical reactivity [*Heiss et al.*, 2017].

Few previous studies, however, considered the effect of temperature differences between groundwater and seawater on coastal aquifer dynamics despite the fact that temperature changes affect physical properties of fluid such as density and viscosity [*Jamshidzadeh et al.*, 2013; *Van Lopik et al.*, 2015]. The co-existence of temperature and salinity gradients prompts double diffusion of heat and salt in coastal aquifers [*Diersch and Kolditz*, 1998]. Due to their distinctly different diffusivities, heat and salt transfer in such circumstances potentially give rise to more complex flow than that under isothermal conditions [*Diersch and Kolditz*, 2002].

Based on satellite-derived land surface temperature data, *Benz et al.* [2017] calculated and reported a global map of estimated groundwater temperature wherein it ranged from the frozen temperature up to 40°C (supporting information Figure S1). While groundwater temperatures are comparatively stable, coastal seawater temperatures can vary seasonally or even daily [Taniguchi, 1993; Anderson, 2005]. For example, the World Ocean Atlas 2013 provided survey data on seawater temperature at various (ocean) depths [*Locarnini et al.*, 2013]. The data show that seawater temperatures varied between 0 and 37°C (supporting information Figures S2-S3). Analyses based on these data of fresh groundwater ($T_f$) and seawater temperatures ($T_s$) revealed a wide range of fresh-saltwater temperature contrasts from -15°C (colder seawater) to 15°C (warmer seawater) along the global coastlines (supporting information Figure S4). Such differences will affect the flow and transport within affected aquifers. Thermal differences between coastal seas and groundwater can, of course, be subject to variations at different time scales. Overall, the hydrodynamics in the intertidal zone are subject to variations of temperature contrast, the duration and extent of which depends on spatial location.

Below, we examine the response of subsurface processes in the intertidal zone to varying freshwater-saltwater temperature contrasts. The research questions addressed are: (1) How do temperature differences affect the USP and saltwater wedge? (2) How does the aquifer-ocean mass exchange vary with different temperature contrasts? and (3) How does the effect of temperature contrast change with different tidal amplitudes?

# 2. Methods

## *2.1. Laboratory experiments*

A 2.2 m × 1.0 m × 0.1 m (length × height × thickness) sand flume was used to investigate the thermal effect at the laboratory scale and to validate a numerical model (Fig. 2a-c). The flume was composed of three chambers including freshwater and saltwater reservoirs on the two ends, with seawater intrusion and circulation in the 1.96-m long central compartment. The three compartments were separated by stainless steel screens to prevent loss of sand from the central compartment. The entire structure was thermally insulated by incorporating a two-layered vacuum tempered-glass chamber as the front wall, and a three-layered polystyrene and extruded polystyrene foam (XPS) wall at the back. The 8-mm XPS layer acted as the heat insulator with a thermal conductivity of 0.035 W/m/°C. Heat conduction through the bottom steel platform was minimized using two layers of aerogel blanket (thermal conductivity of 0.018 W/m/°C). The equipment was situated in an air-conditioned laboratory that was maintained at 25°C.

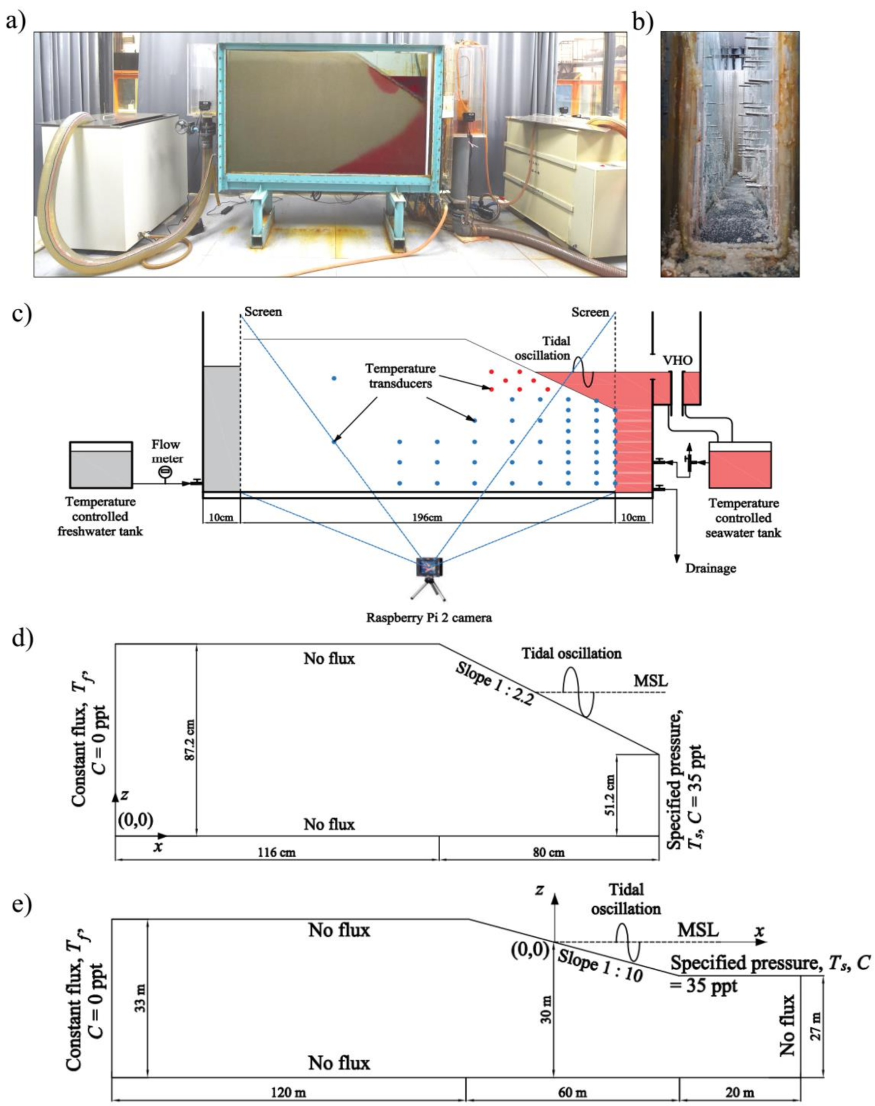


Fig. 2. Physical experiment: laboratory setup (a), temperature sensor installation (b) and schematic diagram of the setup (c). Numerical simulation: laboratory-scale model setup (d), and field-scale model (setup). Salinity ($C$) is 0 ppt and 35 ppt at the landward and seaward boundaries, respectively. Temperatures of freshwater ($T_f$) and seawater ($T_s$) vary depending on the simulation scenarios. VHO is the variable height overflow. MSL is the mean sea level.

The experiment setup involved filling the flume with well-graded quartz sand to the height of 0.9 m with a volumetric porosity of 0.39. Freshwater and saltwater were stored in two temperature-controlled tanks with temperatures monitored continuously. A submerged pump was placed at the bottom of the saltwater tank to maintain the well-mixed condition. A small submerged pump was set up above the freshwater discharge exit to minimize the dilution and maintain the fixed seawater temperature and salinity. FD&C red food dye was mixed with saltwater to visualize the salt front and the USP, the movements of which were captured by a Raspberry Pi 2 camera (resolution 8 MP) during the experiment [*Kuan et al.*, 2012; *Pagnutti et al.*, 2017]. The aquifer temperatures near the seaward boundary and throughout the USP were monitored by multiple waterproof digital thermometers (Dallas Semiconductors DS18B20, resolution of 0.0625°C, accuracy of ±0.5°C [*Rubeis et al.*, 2017; *Zhang et al.*, 2017, 2018]) installed in the back wall (Fig. 2b). Signals from the thermometers were recorded and stored by an in-house developed data logger composed of two microcontrollers (one MEGA and one UNO Arduinos) connected to a Raspberry Pi 3. A flux-controlled condition was applied to the landward freshwater boundary using a flow meter to monitor the influx at the inlet of the freshwater reservoir. The tidal signal was generated using a variable height overflow mechanism at the seaward boundary. The equipment includes a rotating arm connected to the variable-head-oscillating column in the saltwater reservoir and controlled by a DC motor connected to variable power supply (Fig. 2c). The tidal period of 114 s was defined by the rotation rate of the arm. The tidal amplitude of 5.85 cm was adjusted by changing the rotation radius.

Prior to each experiment, the sand flume was flushed continuously for about 30 min to achieve a uniform temperature distribution and then filled fully with deionized water at 25°C to set the initial condition. The saltwater solution was prepared by dissolving sodium chloride (NaCl) and FD&C red food dye in deionized freshwater. The salt concentration of the solution was adjusted by monitoring the fluid density using a high-precision liquid densimeter (accuracy 0.0001 g/cm$^3$, Beijing Yitino Electronic Technology Company). During the experiment, the saltwater density was monitored every 15 min and adjusted by adding a brine stock solution (salinity of 200 ppt) as required.

Two laboratory experiments were conducted for isothermal and warmer seawater conditions. The freshwater entering the landward boundary was set at a constant temperature of 25°C while the saltwater was 40°C in the warmer seawater case. It should be noted that a temperature of 40°C is uncommon for both freshwater and saltwater. In this first attempt to study the thermal effect on coastal aquifers, the temperature range was chosen on the basis of fulfilling the temperature contrast range and the dominant groundwater temperature based on analyzing the global data (supporting information Figures S1-S4). Thus, the full range of temperature contrast from -15 to 15°C was preserved and a $T_f$ value of 25°C was chosen. It is expected that the mechanisms involved in thermal effect and their extent largely depend on temperature contrasts rather than the absolute values of $T_f$ and $T_s$.

### *2.2. Numerical simulations*

The two-dimensional multi-species solute and energy transport model, SUTRA-MS, was used to investigate effects of varying temperatures on the coupled pore-water flow, and heat and salt solute transport in the intertidal zone [*Hughes and Sanford*, 2005; *Voss and Provost*, 2010; *Shen et al.*, 2016]. The model calculates pore-water pressure in porous media by solving:

$$\varepsilon\rho_f \frac{\partial S_w}{\partial p}\frac{\partial p}{\partial t} + \varepsilon S_w\left(\frac{\partial \rho_f}{\partial C}\frac{\partial C}{\partial t} + \frac{\partial \rho_f}{\partial T}\frac{\partial T}{\partial t}\right) - \nabla \cdot \rho_f q = Q_p \tag{1a}$$

$$q = -\left(\frac{kk_r}{\mu}\right)\nabla \cdot \left(p - \rho_f g\right) \tag{1b}$$

where $S_w$ is the water saturation, $\varepsilon$ is the soil porosity, $t$ is the time [T], $C$ is the solute concentration [ML$^{-3}$], $T$ is the fluid temperature [°C], $Q_p$ is the fluid source/sink [ML$^{-3}$T$^{-1}$], $q$ is the Darcy flux [LT$^{-1}$], $k$ is the intrinsic permeability [L$^2$], $k_r$ is the relative permeability for unsaturated flow, $\mu$ is the fluid viscosity [ML$^{-1}$T$^{-1}$], $p$ is the pore-water pressure [ML$^{-1}$T$^{-2}$], $\rho_f$ is the fluid density [ML$^{-3}$] and $g$ is the magnitude of gravitational acceleration [LT$^{-2}$]. It worth noting that the SUTRA-MS model also considers unsaturated flow. The relative hydraulic conductivity and the soil saturation are calculated using the well-known formulas of [*Van Genuchten* [1980].

The governing equations for solute and heat transport are:

$$\frac{\partial \varepsilon S_w \rho_f C}{\partial t} + \nabla \cdot (\rho_f q C) = \nabla \cdot (\varepsilon S_w \rho_f D_m \nabla \mathrm{C}) \tag{2}$$

$$[\varepsilon\rho_f c_f + (1-\varepsilon)\rho_s c_s]\frac{\partial T}{\partial t} + \nabla \cdot (qT) = \nabla \cdot (\lambda_b \nabla T) \tag{3a}$$

$$\lambda_b = \frac{\varepsilon\lambda_f + (1-\varepsilon)\lambda_s}{\varepsilon\rho_f c_f} \tag{3b}$$

where $D_m$ is the molecular diffusivity for salt [L$^2$T$^{-1}$], $c_s$ the specific heat of the porous medium [L$^2$T$^2$°C$^{-1}$], $c_f$ is the specific heat of fluid [L$^2$T$^2$°C$^{-1}$], $\lambda_b$ is the bulk thermal diffusivity of the saturated porous media [$L^2T^{-1}$], $\lambda_f$ is the thermal conductivity of fluid [$MLT^{-3}$°$C^{-1}$] and $\lambda_s$ is the thermal conductivity of solid [$MLT^{-3}$°$C^{-1}$].

The numerical model source codes were modified to incorporate the following non-linear relation of density with salt content and temperature [*Van Lopik et al.*, 2015]:

$$\rho_f(T,C) = (999.9 + 2.034\times10^{-2}T - 6.162\times10^{-3}T^2 + 2.261\times10^{-5}T^3 - 4.657\times10^{-8}T^4) + (0.802C - 2.001\times10^{-3}CT + 1.677\times10^{-5}CT^2 - 3.06\times10^{-8}CT^3 - 1.613\times10^{-8}C^2T^2) \quad (4)$$

Fluid viscosity ($\mu$) is a function of temperature and was calculated by the model following [*Hughes and Sanford*, 2005]:

$$\mu = 239.4\times10^{-7}\times10^{\frac{248.37}{T+133.15}} \quad (5)$$

The sinusoidal tidal signal was generated as follows:

$$H_{sw}(t) = H_{\mathrm{MSL}} + A_T\sin(\omega t) \quad (6)$$

where $H_{SW}$ is the water level, $H_{\mathrm{MSL}}$ is the mean sea level [L], $A_{\mathrm{T}}$ is the tidal amplitude [L] and $\omega = 2\pi/P$ is the angular frequency [$T^{-1}$] with $P$ being the tidal period [T].

Fig. 2b presents the domain and setup for the laboratory-scale simulation, which aimed to replicate the experiments. The finite-element mesh constructed by SutraPrep (a pre-processor of the SUTRA model) had flexible element size that fitted to the domain outline. The mesh was coarser at the inland subdomain and more refined at the intertidal and seabed subdomain (Table 1). A flux-controlled condition was applied at the inland boundary while the seaward boundary was subjected to the tidal oscillations. A similar treatment of the seaward boundary condition to *Xin et al.* [2010] was adopted wherein hydrostatic pressure was specified for the submerged nodes (below the sea surface). The code was programmed to calculate and apply the hydrostatic pressure for these nodes at each time step. For nodes above the sea level, the local pressure was either reset to atmospheric pressure ($P$ = 0) or removed (became no flow) depending on whether it was saturated or unsaturated in the previous time step. The top and bottom boundaries were both set as zero flux. The upscaled version of the model (Fig. 2c) simulated a shallow unconfined aquifer following *Xin et al.* [2010]. This aquifer had a thickness of 33 m and a total length of 200 m including 150 m landward extent and 50 m seaward extent from the shoreline. Similar boundary conditions to those of the laboratory-scale model were applied to the field-scale model except for the seaward vertical boundary, which was also set to zero flux. Typical parameter values for heat and solute transport were used for both laboratory and field-scale models, including the molecular diffusivity ($D_m$ = $10^{-9}$ $m^2/s$), the thermal conductivity of fluid ($\lambda_f$ = 0.6 W/m/°C) and solid ($\lambda_s$ = 3.5 W/m/°C), the specific heat of fluid ($c_f$ = 4182 J/kg/°C) and solid ($c_s$ = 840 J/kg/°C) [*Hughes and Sanford*, 2005; *Voss and Provost*, 2010; *Kuan et al.*, 2012; *Lee*, 2012; *Jamshidzadeh et al.*, 2013]. The *Van Genuchten* [1980] soil water retention parameters for laboratory scale simulations were adopted from *Xin et al.* [2018] who used the same sand for their experiment (the residual water saturation $S_{Wres}$ = 0.05, $\alpha$ = 11 $m^{-1}$ and $n$ = 6). For field-scale simulations, the typical values for coastal sand from *Carsel and Parrish* [1988] were used ($S_{Wres}$ = 0.1, $\alpha$ = 14.5 $m^{-1}$ and $n$ = 2.68). Other scale-dependent parameters along with modeling scenarios are listed in Table 1.

**Table 1: Modeling parameters for laboratory and field-scale simulations**.

| | **Laboratory-scale model** | **Field-scale model** |
|---|---|---|
| *Mesh size and time step* | | |
| Inland subdomain (m) | $\Delta x$ = 0.008<br>$\Delta z$ = 0.0039 | $\Delta x$ = 1.33<br>$\Delta z$ = 0.14 |

| | | |
|---|---|---|
| Intertidal and seabed subdomain (m) | $\Delta x$ = 0.004<br>$\Delta z$ = 0.0024~0.0039<br>(varying from seaward to inland boundary) | $\Delta x$ = 0.25<br>$\Delta z$ = 0.14 |
| Time step (s) | 2 | 30 |
| *Properties of porous medium* | | |
| Porosity, $\varepsilon$ | 0.39 | 0.45 |
| Intrinsic permeability, $k$ ($m^2$) | $5 \times 10^{-10}$ * | $1.157 \times 10^{-11}$ |
| Longitudinal dispersivity, $\alpha_L$ (m) | 0.0004 | 0.5 |
| Transverse dispersivity, $\alpha_T$ (m) | 0.00004 | 0.05 |
| *Boundary conditions* | | |
| Freshwater flux, $q_f$ ($m^3$/s) | $0.33 \times 10^{-6}$ | $2.81 \times 10^{-6}$ |
| Mean sea level, $H_{MSL}$ (m) | 0.7 | 0 |
| Tidal amplitude, $A_T$ (m) | 0.0585 | 1 |
| Tidal period, $P$ (s) | 114 | 43200 |

* Fitted value with temperature-dependent hydraulic conductivity determined empirically.

Two scenarios of thermal contrast – isothermal and warmer seawater – identical to those of the physical experiments were simulated at the laboratory scale (Table 1). Although the sand flume was designed to minimize the heat dissipation, lateral heat loss still took place. In the simulations, the heat loss was considered by setting a heat flux boundary calculated by the product of a thermal conductance (applied at each node of the domain) and the room/sand flume temperature variance. The SUTRA-MS model was then calibrated by changing the thermal conductance and comparing the simulated temperature and salt distribution patterns with measured results. Afterward, the model was employed systematically to further explore changes in pore-water flow and salinity distribution under different temperature contrasts ($\Delta T = T_s - T_f$) and tidal amplitude ($A_T$). Comparisons were made among the three representative cases for colder seawater, isothermal and warmer seawater conditions, with the tidal amplitude of 1 m and temperature contrast of -15°C ($T_s$ = 10°C), 0°C ($T_s$ = 25°C) and 15°C ($T_s$ = 40°C), respectively. Then, an in-depth quantitative analysis was carried out using results for the entire range of temperature contrast from -15°C to 15°C and varying amplitude from 1 m to 2 m. The field-scale simulations were conducted in a similar manner, except that no lateral heat loss was considered.

# 3. Results

## *3.1. Model validation at the laboratory scale*

The saltwater distribution captured experimentally by the camera was compared with the simulated results for the isothermal condition (Fig. 3a) and the non-isothermal condition with seawater 15°C warmer than freshwater (Fig. 3b). With the tidal fluctuations, a USP [*Robinson et al.*, 2007] was formed in the intertidal region above the lower saltwater wedge. The model captured well the extension of the lower saltwater wedge and the USP in both cases although the width of the mixing zone due to hydrodynamic dispersion could not be visualized well by food dye [*Goswami and Clement*, 2007; *Chang and Clement*, 2012; *Kuan et al.*, 2012; *Abdoulhalik and Ahmed*, 2018]. In comparison to the isothermal condition, the toe of the saltwater wedge retreated seaward by approximately 20 cm when seawater was warmer (Fig. 3c). Based on equation (4), the density of seawater at 40°C was about 5.3 kg/m$^3$ less than that at 25°C, which explains the seaward withdrawal of the saltwater wedge. It is noteworthy that warmer seawater appeared to broaden the lower mixing zone slightly compared to the isothermal case. This might be due to the opposite density gradients caused by the salt and temperature distributions. In addition to the seaward density gradient associated with the salinity change near the freshwater-saltwater interface as in the isothermal condition, the increase of temperature seaward produced a landward density gradient near the seaward boundary, providing a double-diffusive convection mechanism that expanded the lower mixing zone. A slight expansion of the USP was observed with warmer seawater, likely due to the withdrawal of the lower saltwater wedge. The field-scale simulation results will elaborate further the behaviors of this zone in response to aquifer-ocean temperature differences.

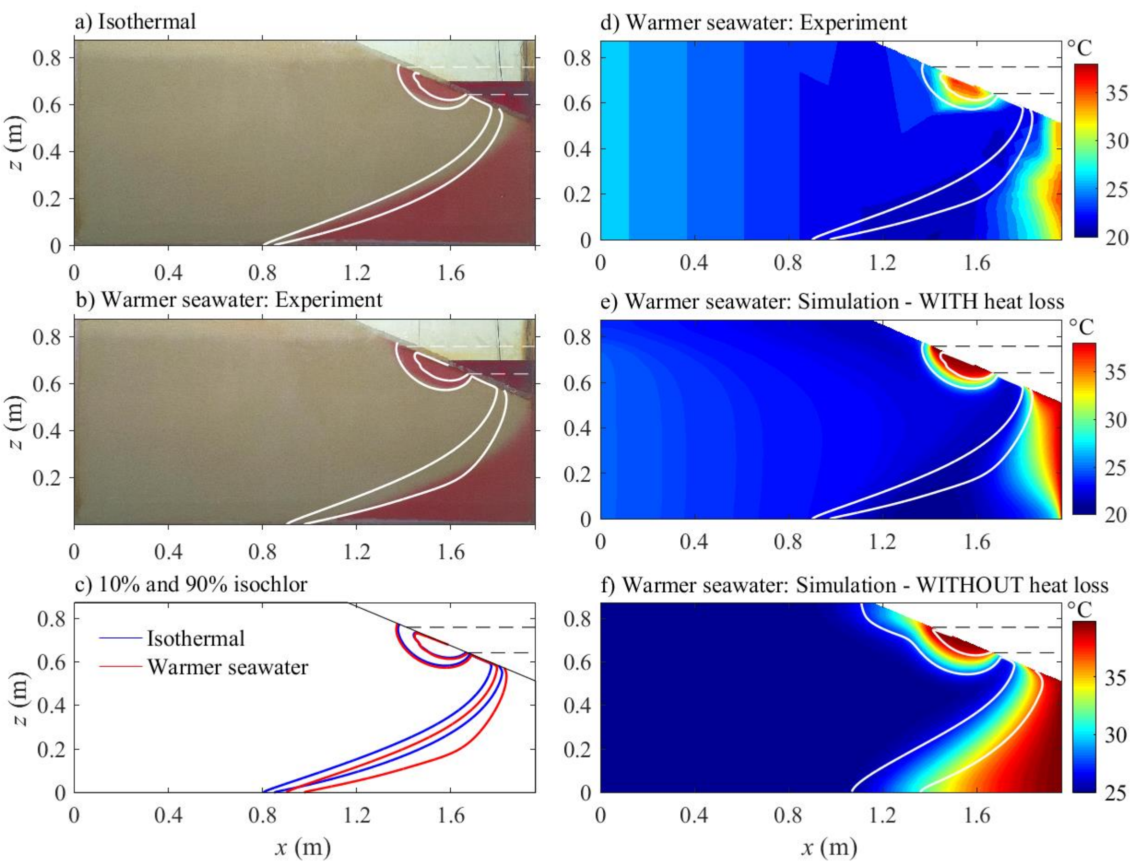


Fig. 3. Results of salinity (a-c) and temperature (d-f) distributions obtained from the laboratory observations and laboratory-scale modeling for the cases of isothermal and warmer seawater. The white lines represent 10% and 90% isohalines extracted from the

numerical simulations of the corresponding scenarios. The dashed lines indicate the high and low tide levels.

Figs. 3d-f present the patterns of temperature distribution obtained from physical experiments and simulations. Two separated temperature transition zones (where temperature varied between $T_f$ and $T_s$) were captured, one near the beach surface driven by the tidal forcing and the other at the bottom right corner formed by density-driven saltwater circulation. Two laboratory-scale numerical simulations are displayed: one considered lateral heat loss (Fig. 3e) and the other ignored it (Fig. 3f). Agreement between the simulations and experiment results was obtained when the conductance of the lateral heat loss was set to 0.0002°C/s. Distinct temperature patterns were observed in the cases with and without lateral heat loss considered. When heat loss was considered, although the heated region could extend to the saline lower mixing zone (Fig. 3d), the temperature transition zone resided predominantly at the narrow proximity of the offshore vertical boundary. Without heat loss, the thermal pattern in the saltwater wedge more or less replicated the salinity distribution (Fig. 3f). This result reflected the importance of heat dissipation in correctly interpreting subsurface flows under the seabed.

### *3.2. Temperature effect on salinity distribution: Field-scale simulations*

The effects of temperature contrast on flow and transport in shallow coastal aquifers were explored further through the field-scale numerical simulations. In all the simulation scenarios, the freshwater temperature was kept constant at 25°C. Three representative cases of isothermal, warmer and colder seawater conditions were considered, with seawater temperature set at 25, 40 and 10°C, respectively. By assuming uniformity in the alongshore direction, no lateral dissipation of heat was included in the simulation.

Fig. 4 presents the quasi-steady and phase-averaged (averaged over a tidal cycle) distribution of salt over the field-scale domain predicted by the numerical model. As expected, colder seawater enhanced seawater intrusion and warmer seawater reduced it as evident in comparison with the isothermal condition. Moreover, it is noteworthy that for the same temperature contrast (15°C), the intrusion enhancement from the colder seawater was much less significant compared to impediment from the warmer seawater. Fig. 4d shows a comparison of the 10% and 90% isohalines obtained from all three cases. The lower salt front (10% isohaline) retreated by a distance approximately 7 m from 19.1 m from the shoreline in the isothermal case to 12.2 m with warmer seawater whereas it advanced 4 m landward with colder seawater (to 23 m).

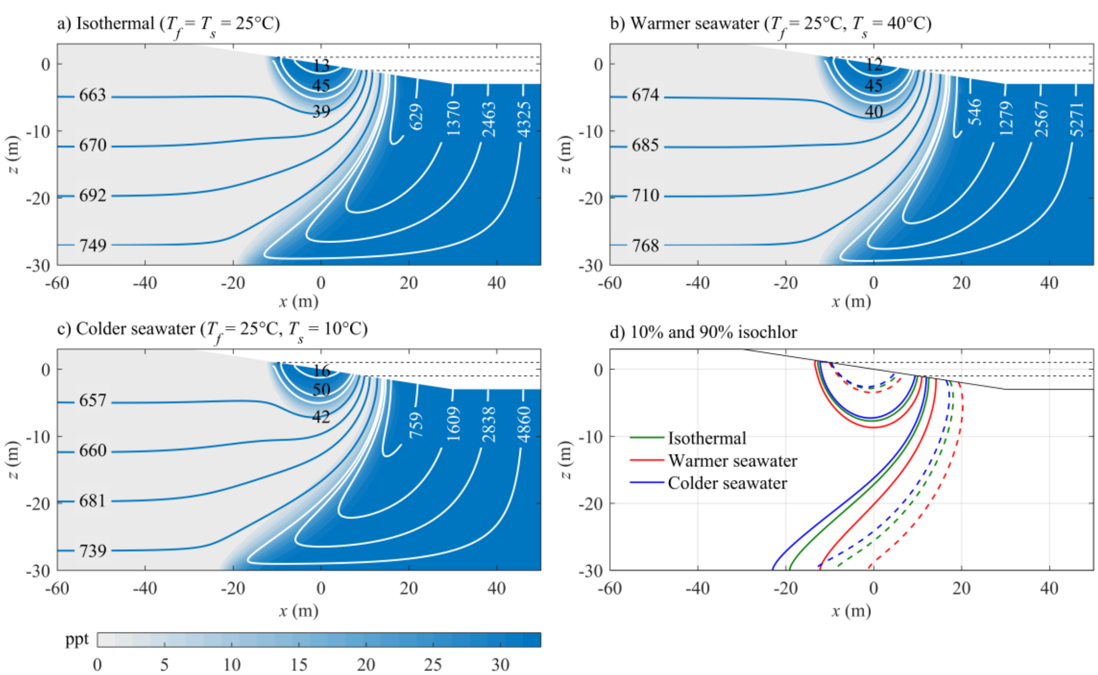


Fig. 4. Modeling results (phase-averaged) for salinity distributions (color contour), flow paths (solid lines) and travel time (numbers – in days) (a-c). The cases are indicated in

the figure titles. For comparison, the 10% (solid) and 90% (dashed) isohalines from the three cases are given in (d). The horizontal black dashed lines indicate the high and low tide levels.

For the non-isothermal cases, the distribution patterns of temperature and hydraulic conductivity are presented in Fig. 5. In comparison with the saline lower mixing zone, the thermal transition zone in the saltwater wedge was much more dispersive, spreading over a distance up to 50 m of the aquifer base in both cases due to the larger diffusivity of heat. Moreover, unlike the relatively even width of the saline lower mixing zone, the temperature distribution expanded rapidly over depth in the aquifer. The trend could be observed more clearly in the warmer seawater condition than the colder case. Such a variation in the distribution of salt and heat increased the complexity of the density distribution in the saltwater wedge and hence impacted the pore water flow. The wider thermal transition zone reduced the density gradient in the saltwater wedge in the warm seawater case but increased it in the cold seawater case. Therefore, the pore water flow weakened in the former case and was strengthened in the latter. Furthermore, the pattern of hydraulic conductivity variation replicated closely that of heat. The seawater at 25°C had a hydraulic conductivity of 11.28 md$^{-1}$. The 40°C seawater boundary raised the hydraulic conductivity throughout the saltwater wedge by up to 1.5 times to approximately15 md$^{-1}$ but decreased by 25% to less than 8 md$^{-1}$ for the case with the $T_s$ lowered to 10°C.

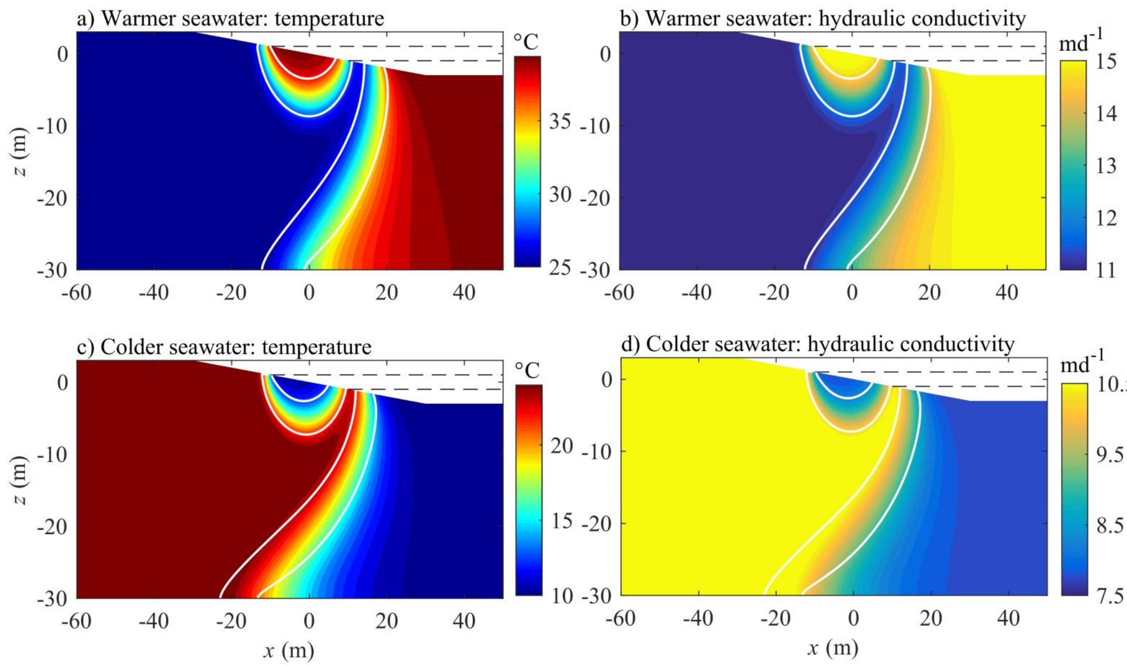


Fig. 5. Modeling results (phase-averaged) for the distributions of temperature (left panel) and hydraulic conductivity (right panel) in the two non-isothermal cases of (a, b) warmer seawater ($T_f$ = 25°C, $T_s$ = 40°C), and (c, d) colder seawater ($T_f$ = 25°C, $T_s$ = 10°C). The solid white lines are 10% and 90% isohalines. The black dashed lines at the beach surface indicate the high and low tide levels.

The USP was formed near the sloping surface in all cases regardless of seawater temperature. However, different from the saltwater wedge, the USP and upper mixing zone expanded strongly with warmer seawater and reduced slightly with colder seawater (Fig. 4d). The seawater at 40°C enlarged the USP area (calculated as the area from the 10% isohaline to the seaward boundary) to 102 $m^2$ compared with 82.7 $m^2$ for the isothermal case, an increase of 23%. With a similar 15°C temperature difference, the cold seawater case ($T_s$ = 10°C) generated a contraction of only 10% (to 74.5 $m^2$), indicating again a greater impact due to warmer seawater compared with its colder counterpart, on both the tidal seawater circulation near the beach surface and density-driven circulation in the saltwater wedge.

The opposite behaviors of the saltwater wedge and the USP reflects the strong hydrological connection between oceanic forcing and seawater intrusion as previously reported [*Kuan et al.*, 2012; *Xin et al.*, 2014]. Expansion of the USP in the warmer seawater case was associated with seaward movement of the saltwater wedge due to the thermally induced decrease of saltwater density and vice versa. This consistency was confirmed through the harmonious variation of the area of the saltwater wedge (reduction) and the USP (growth) as a function of seawater temperature and fresh-saltwater temperature contrast (Fig. 4d). In the USP, a similar disparity could be observed between the saline upper mixing zone and the temperature transition zone as in the lower interface of the saltwater wedge.

### ***3.3.Temperature effect on seawater circulation: Field-scale simulation***

The flow paths and travel times of particles within the subterranean estuary were calculated based on the phase-averaged pore-water flow field (the local velocities were averaged over a tidal cycle) [*Robinson et al.*, 2007; *Xin et al.*, 2010]. For the freshwater zone, the particles were released uniformly at $x$ = -120 m, whereas for the seawater they started at the seaward boundary. The travel time measured the time taken for particles to leave the aquifer. Under tidal forcing, the coastal aquifer was divided into three separate zones (Fig. 4), i.e., the USP, saltwater wedge and freshwater discharge zone, with distinct flow paths of either freshwater or seawater as reported previously [*Robinson et al.*, 2007; *Xin et al.*, 2010]. Near the beach surface, saltwater entered the aquifer at the upper intertidal zone and seeped out at the lower intertidal zone. Despite the larger USP and thus longer flow paths, the warmer seawater case shows similar travel times for tidal seawater circulation to that under isothermal conditions. The colder seawater, on the other hand, notably lengthened the average residence time. Both effects were linked to the thermally induced variation of hydraulic conductivity in the USP. The faster saltwater passing through the USP for increased seawater temperature would promote more contact between land-sourced chemicals and marine-based ones.

The terrestrial freshwater, which followed horizontal flow paths towards the sea, was confined between the USP and the saltwater wedge. The calculated travel time shows a slight reduction with colder seawater due to the shortened flow paths. Overall, the freshwater flow was less affected by heat gradients that existed mainly in the saltwater zone.

A more complex thermal influence was observed in the lower section of the saltwater wedge. Saltwater entered the aquifer vertically from offshore and arrived at the lower section of the lower mixing zone. Driven by the freshwater head gradients, the lower mixing zone diverted the flow direction upward with saltwater circulating back to the ocean in the nearshore region. The longer flow paths in the colder seawater case prolonged the transit time of the seawater particles in comparison to the isothermal case.

With warmer seawater, the thermal effect on seawater circulation diverged between particles entering the domain from either the sloping beach surface or the flat seabed. For the former, the transit time was significantly reduced due to shorter pathways compared to the isothermal condition. For the latter, however, an unexpected increase of the transit time was evident with an increase of hundreds of days in spite of the shorter pathway. This was due to the dissimilarity of salinity and temperature distribution patterns, which directly affected pore water flow in this area. Unlike the isothermal case where significant variations of seawater density occurred only within the lower mixing zone, the presence of heat gradients allowed density variations across the entire saltwater wedge, creating opposite effects on the pore water flow in colder and warmer seawater cases. With colder seawater, the thermally induced density gradient (density variation caused by the temperature gradient alone) was in the same direction as that of the salinity-induced density gradient and thus it amplified landward motion of seawater. With warmer seawater, the two density gradients acted in opposite directions, especially in the deep area. As a result, the landward flow was significantly retarded by the temperature gradient. As the temperature gradient prevailed in the lower section of the saltwater wedge (Fig. 4b), the retarded effect was most evident for the saltwater paths that originated from the seabed. The flow paths originating from the sloping surface were less affected.

To separate the individual effects of temperature on fluid density and viscosity, we ran three additional simulations with a constant viscosity (Fig. 6). The thermal change of viscosity has a much larger impact on the hydraulic conductivity compared to that of density. Within the temperature range of this study (from 10 to 40°C), the hydraulic conductivity deviated only 0.05 m/d (by 0.5%) from the value at 25°C when a constant dynamic viscosity was applied. The additional simulations were performed with the viscosity of freshwater at 25°C (0.00089 N.s/$m^2$). Major changes were observed with the transit time of saltwater through the USP and the saltwater wedge in both non-isothermal cases (Fig. 6a, b). The saltwater particles remained slightly longer in the domain in the warmer seawater case as a result of the reduced hydraulic conductivity. With colder seawater, the transit times were reduced by up to 25% due to increased hydraulic conductivity. The effect was more clearly observed with the particles entering the saltwater wedge near the vertical boundary. No significant change was observed for the residence time of freshwater. These results demonstrated a restraint of landward flow by the thermally variable hydraulic conductivity in colder seawater case and an improvement in warmer seawater case. On the other hand, the hydraulic conductivity change had only a minor effect on the extent of saltwater intrusion as represented by position of the 10% and 90% isohalines (Fig. 6c, d). This suggests saltwater intrusion is mainly dependent on the fresh-saltwater density contrast.

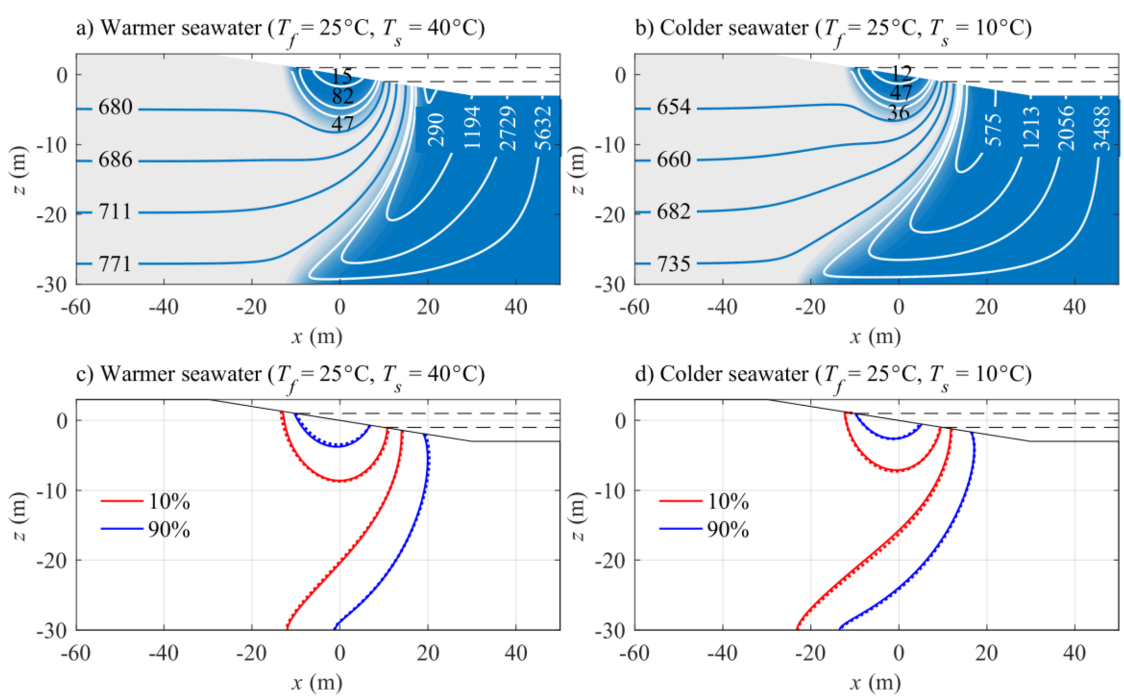


Fig. 6. Modeling results (phase-averaged) of salinity distribution (color contour), flow path (solid lines), and travel time (numbers – in days) in the non-isothermal cases simulated with fixed viscosity (a-b). Comparison of the 10% (red) and 90% (blue) isohalines in fixed (solid) and thermally dependent (dotted) viscosity (c-d). The cases are

indicated in the figure titles. The horizontal black dashed lines indicate the high and low tide levels.

In terms of material exchange across the aquifer-ocean interface, the simulation results indicated a major intensification of phase-averaged fluxes of water and salt when seawater was 15°C warmer than freshwater (Fig. 7). The most significant enhancement was observed with the tidally driven influx. The total volume of seawater flowing across the USP increased by 36.3% from 1.55 $m^3$/m/d in the isothermal condition to 2.1 $m^3$/m/d. The total efflux of both fresh and saline water, i.e., the SGD, was also intensified by warmer seawater, rising from 4.28 $m^3$/m/d to 4.8 $m^3$/m/d, equivalent to an increase of 12.3%. With colder seawater, the land-ocean exchange of water and solute decreased. Again, the warmer seawater exerted a more profound effect than the colder seawater despite the same magnitude of temperature difference. It was clear from the simulated results that the freshwater-saltwater temperature contrast influenced the configuration of the coastal aquifer and aquifer-ocean dynamics to an extent associated directly with its magnitude.

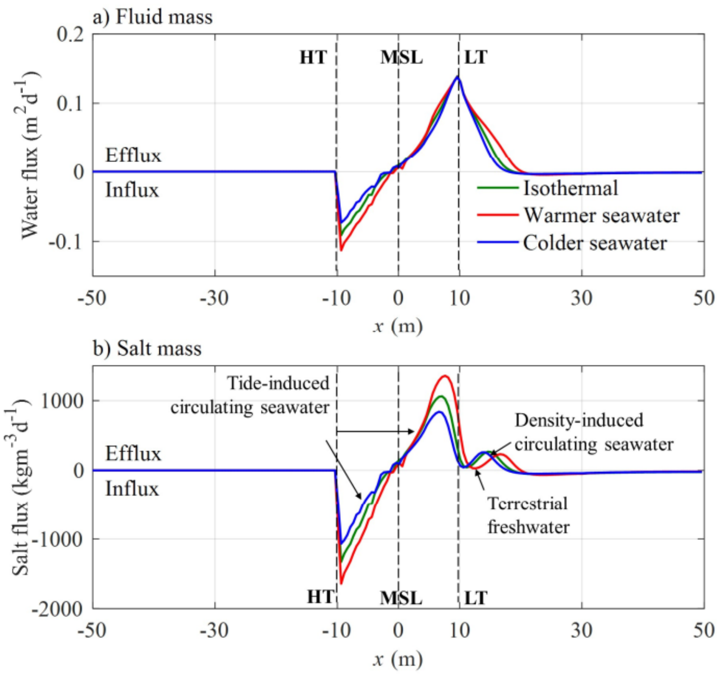


Fig. 7. Comparison of per unit area (a) water fluxes and (b) salt fluxes across the beach surface under the three conditions: isothermal ($T_f = T_s = 25°C$), warmer seawater ($T_f = 25°C$, $T_s = 40°C$) and colder seawater ($T_f = 25°C$, $T_s = 10°C$). MSL, HT and LT indicate the mean sea level, high tide and low tide levels, respectively.

### *3.4. Sensitivity analysis of temperature contrasts*

Fig. 8 summarizes the modeling results of four different spatial parameters representing the aquifer configuration observed over a range of temperature contrasts from -15°C (colder seawater) to 15°C (warmer seawater) (the freshwater temperature was fixed at 25°C). The relative change relative to the isothermal case was calculated. As the temperature contrast increased from -15 to 15°C, the saltwater wedge area contracted, i.e., the relative change decreased from 4.1% to -8.6% (Fig. 8a). However, opposite trends were observed for the thermal effect on the saltwater wedge toe position and the USP area (Figs. 8b, c). For both, the relative changes increased as the temperature contrast increased. The increase in the position of the saltwater wedge toe reflected further seawater intrusion and was consistent with the increased saltwater wedge area. Overall, the range of the relative change (from -5% to 13%) was significantly less than that for the USP (-10% to 22%).

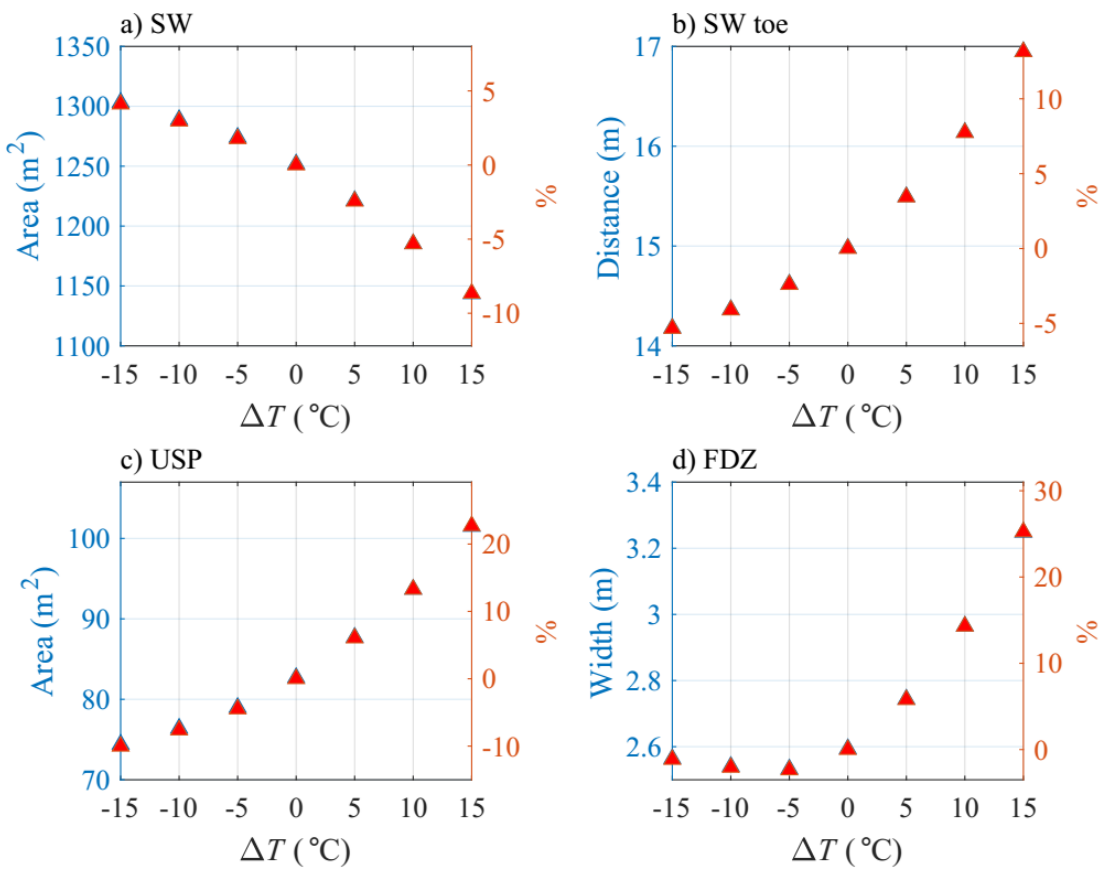


Fig. 8. Modeling results for (a) area of the saltwater wedge (SW), (b) position of the SW toe from the shoreline (represented by the 10% isohaline), (c) area of the upper saline plume (USP), and (d) width of the exit of the freshwater discharge zone (FDZ - distance between the 10% isohalines of the USP and the SW) over the range of temperature contrast from -15°C (colder seawater) to 15°C (warmer seawater). The right axis indicates the percentage of relative change of corresponding parameter compared to the value for isothermal conditions.

The dynamic coupling of the upper and lower salt fronts defined the behavior of the freshwater discharge occurring between them. The different extents at which the USP and saltwater wedge responded to temperature contrasts modified the exit width of the freshwater discharge zone (calculated as the distance between the ends of the 10% isohalines of the USP and the saltwater wedge at the sloping surface). Fig. 8d presents a non-monotonic trend of the exit width of the freshwater discharge zone. It decreased as the temperature contrast increased from -15 to -5°C and then started to increase. The relative difference reached 25% at the temperature contrast of 15°C. It appeared that the USP contracted at a larger rate than the saltwater wedge retreat for the colder cases but at a lower rate for the warmer cases. Consequently, the exit width of the freshwater discharge zone expanded strongly with warmer seawater and shrank slightly with colder seawater.

With regards to the temperature effects on the aquifer-ocean exchange, the variation of various fluxes as a function of temperature contrast was examined (Fig. 9). As the inland boundary was flux-specified, the freshwater recharge averaged over a tidal cycle was not affected by the tidal fluctuation. At quasi-steady state, the SGD was equivalent to the total inflow into the aquifer including the inflow of saltwater at the upper intertidal region that forms the USP ($Q_t$), the inflow of saltwater at the seabed that contributes to the saltwater wedge ($Q_d$) and the constant freshwater recharge at the flux-controlled inland boundary ($Q_f$). The magnitude of the temperature effect was quantified by computing the phase-averaged influxes of saltwater via the USP ($Q_t$) and the saltwater wedge ($Q_d$) along with the total SGD, which comprised effluxes of fresh and saline waters to the sea ($Q_f$). Afterwards, the thermally variable contribution of tidal forcing and density contrast to the total groundwater discharge was examined. Following *Robinson et al.* [2007], the percentages of tide-induced seawater circulation (TSC) and density-induced seawater circulation (DSC) in the total SGD at varying temperature contrasts were computed as:

$$TSC = \frac{Q_t}{Q_t + Q_d + Q_f} 100 = \frac{Q_t}{SGD} 100 \quad (7)$$

$$DSC = \frac{Q_d}{Q_t + Q_d + Q_f} 100 = \frac{Q_d}{SGD} 100 \quad (8)$$

Fig. 9a demonstrates a steady increase of the SGD with increasing temperature contrast. The variation for the positive contrast range appeared slightly larger than its negative counterpart. An increase of approximately 0.53 $m^3$/m/d (equivalent to 12.3%) was evident over the warmer seawater case range while a reduction 0.39 $m^3$/m/d (equivalent to 9.1%) occurred over the colder seawater range with the same temperature difference of 15°C. A major proportion of the enhancement of SGD was attributed to the increase of seawater circulation within the USP ($Q_t$). With 40°C seawater, $Q_t$ increased by 0.55 $m^3$/m/d, equivalent to 35.6% of the seawater flux in the isothermal case while seawater at 10°C resulted in a decrease by 0.37 $m^3$/m/d, equivalent to 23.6% of that in the isothermal condition (Fig. 9b). The flow intensified increasingly with seawater temperature, responding directly to the thermally variable area of the USP. Meanwhile, the seawater inflow through the seabed ($Q_d$) exhibited a non-monotonic and convex trend with respect to the temperature contrast and peaked at the 0°C difference (Fig. 9c). $Q_d$ remained unchanged at ±5°C difference but decreased quickly by up to 10% for a ±15°C difference. This reduction likely resulted from reduced inflow area for the warmer seawater case and smaller hydraulic conductivity for the colder seawater case.

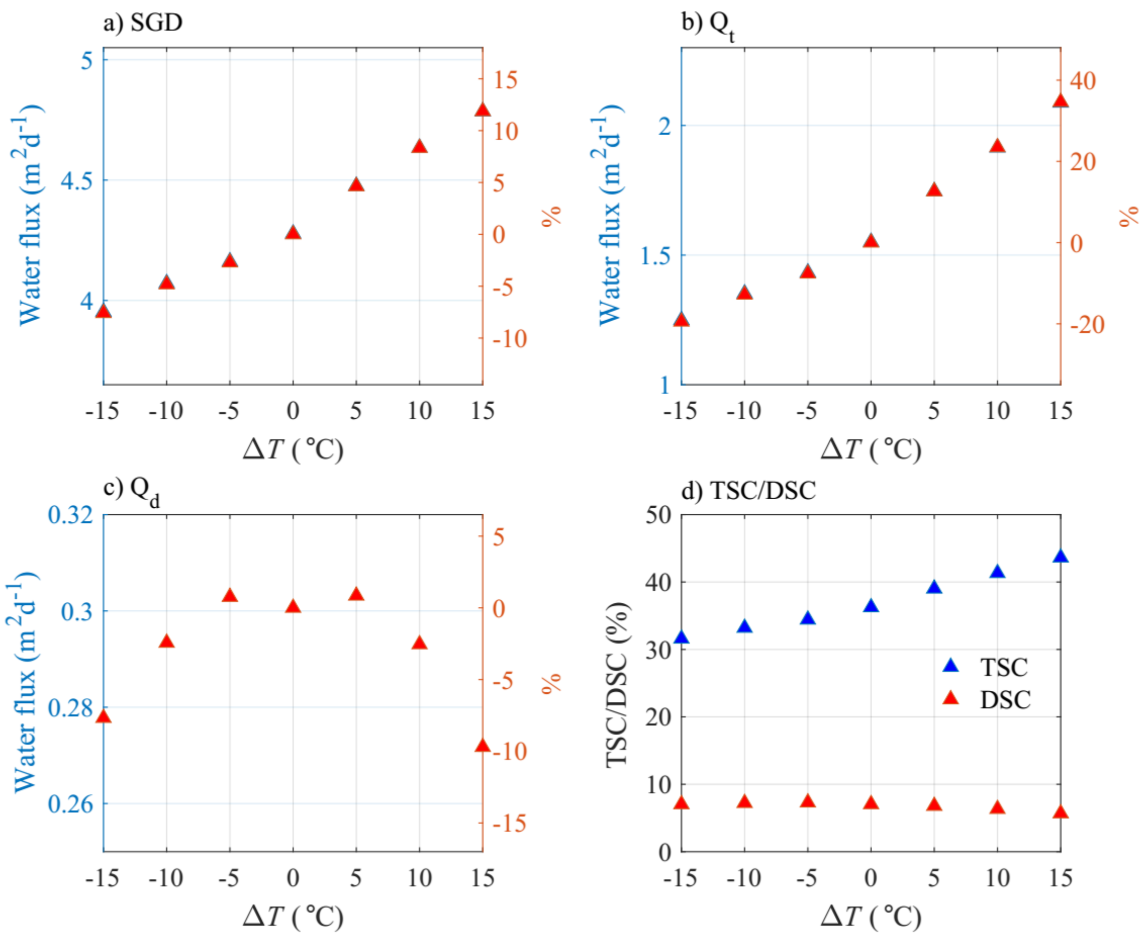


Fig. 9. Modeling results for phase-averaged values of (a) submarine groundwater discharge (SGD), (b) tide-induced seawater circulation ($Q_t$), (c) density-driven seawater circulation ($Q_d$), and (d) percentage of tide-induced seawater circulation (TSC – blue) and density-driven seawater circulation (DSC – red) in the total SGD. The right axis in subfigures (a), (b) and (c) indicates the percentage of change of corresponding parameter relative to the isothermal case.

In Fig. 9d, a shift in the contributions of tidally-induced (TSC) and density-induced (DSC) seawater circulation to total SGD under varying temperature contrasts was demonstrated. A minor fluctuation was present for the DSC around the value of the isothermal case, at 7.0% with a mild reduction to 5.7% for seawater at 40°C. Meanwhile, the TSC increased proportionally to seawater temperature, rising from 30.5% at 10°C to 43.8% at 40°C while the value was 36.3% for isothermal conditions. It was clear that as the seawater warms up, the seawater circulation in the saltwater wedge weakened but that in the intertidal zone intensified. With a negative temperature contrast, the opposite trend was evident.

### *3.5. Sensitivity analysis of tidal amplitude*

The temperature effects were further investigated with tidal amplitudes ($A_T$) changed from 1 m to 1.5 and 2 m. The case with a 1-m tidal amplitude represented the base case as presented in the previous sections. The results (Fig. 10) show that intensive tidal oscillations of the sea level generate a larger USP in the intertidal zone and push the saltwater wedge further seaward [*Kuan et al.*, 2012; *Yu et al.*, 2019b]. This was confirmed by the modeling results of areas of the USP and saltwater wedge shown in Fig. 10a, b. For the three tidal amplitudes, major characteristics of the coastal aquifer remained the same, namely, contraction of the saltwater wedge and expansion of the USP as seawater warmed up. The saltwater wedge contraction, USP expansion and the exit width of the freshwater discharge zone demonstrated similar trends as the associated lines were largely parallel for the three tidal amplitudes.

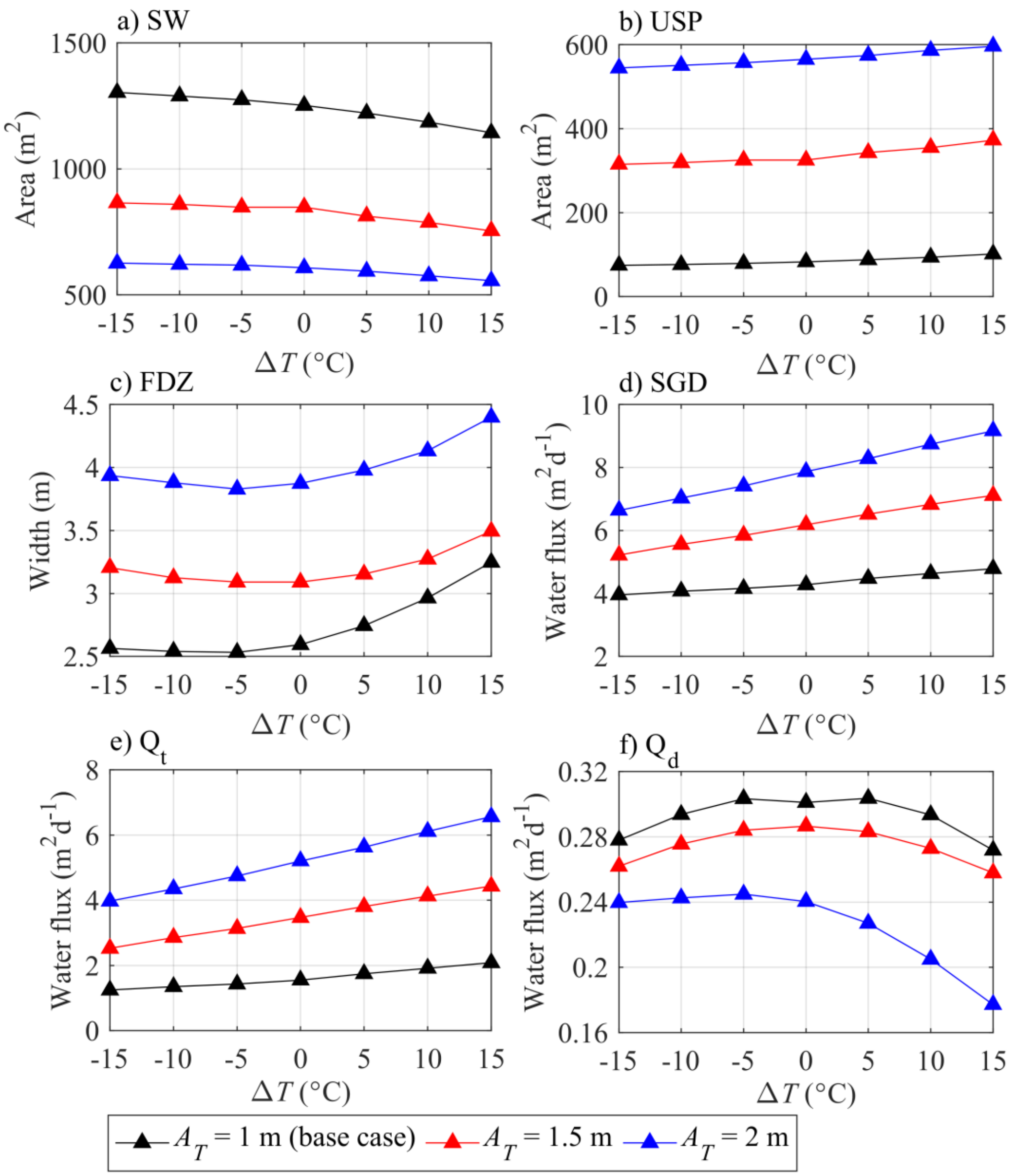


Fig. 10. Variation as a function of temperature contrast of (a) area of the saltwater wedge (SW), (b) area of the upper saline plume (USP), (c) width of the exit of the freshwater discharge zone (FDZ - distance between the 10% isohalines of the USP and the SW), (d) submarine groundwater discharge (SGD), (e) tide-induced seawater circulation ($Q_t$) and (f) density-driven seawater circulation ($Q_d$).

On the other hand, the temperature effect on flow across the subterranean estuary was significantly amplified by an increased tidal amplitude. The linear SGD-$\Delta T$ relationship remained in all cases while the specific rate at which SGD rose with $\Delta T$ increased quickly with the tidal amplitude, by threefold from 0.028 m$^2$/d/°C with $A_T$ = 1 m to 0.084 m$^2$/d/°C with $A_T$ = 2 m (Fig. 10d). Likewise, the intensification rate of the tidally driven seawater circulation ($Q_t$) rose strongly with the expanded tidal range, from 0.028 to 0.086 m$^2$/d/°C for tidal amplitudes of 1 m and 2 m, respectively (Fig. 10e).

The dominant contribution of $Q_t$ to the total SGD remained unchanged regardless of the magnitude of the tidal forcing and temperature contrast (Fig. 10e). Conversely, the density-driven seawater circulation ($Q_d$) underwent more irregular changes in response to the temperature effect with stronger tidal forcing (Fig. 10f). The trend of $Q_d$ changing with $\Delta T$ remained more or less similar with the amplitudes of 1 and 1.5 m. The thermally induced change of $Q_\mathrm{d}$ was rather complex depending on the temperature and hydraulic conductivity distribution within the domain. A slight stagnation observed at $\Delta T$ = 0°C and $A_T$ = 1 m was likely due to different responses of the system to small $T_s$ changes. The decrease of $T_s$ increased the amount of seawater entering the domain by increasing hydraulic gradient whereas the small increase of $T_s$ raised the hydraulic conductivity and allowed a larger influx. With $A_T$ = 2 m, the colder seawater hardly affected $Q_d$ regardless of the temperature difference whereas the warmer seawater reduced $Q_d$ in a more profound way (Fig. 10f). This special feature, however, was unrealistic due to the exceedingly large tidal amplitude that pushed the saltwater wedge all the way to the offshore vertical boundary. Despite that, the general $Q_d$ -$\Delta T$ relationship was confirmed by other cases; specifically, the isothermal condition yielded the largest $Q_d$ while the existence of a temperature contrast resulted in its reduction.

## 4. Discussions

The primary effect of the freshwater-seawater temperature contrast is manifested in the extent of saltwater intrusion. The location of the saltwater wedge toe is a key indicator of the threat posed by seawater intrusion to freshwater resources. Therefore, understanding the effect of the temperature contrast would improve accuracy of the assessment of seawater intrusion for the purpose of coastal freshwater resources management. From the foregoing results, the level and tendency of the thermal impact relate directly to the magnitude as well as direction of the temperature contrast, i.e., whether seawater is colder or warmer than groundwater.

Along with modifying the lower saltwater wedge, the thermal gradient alters the spatial expansion of the upper circulation cell in the intertidal zone. Warmer seawater broadens the USP whereas colder seawater reduces its size. The USP expands/contracts at a rate proportionately related to the saltwater wedge movement and the seawater density variation as a function of temperature difference. The USP is a relatively reactive zone where multiple biogeochemical transformations of land- and marine-sourced chemical compounds would occur [*Slomp and Van Cappellen*, 2004; *Santos et al.*, 2008; *Charbonnier et al.*, 2013; *Anwar et al.*, 2014]. These include inorganic and organic compounds of terrestrial and oceanic origins whose chemical reactivity would be either beneficial or detrimental to the marine ecosystem. Residual nitrate and phosphate compounds from agricultural activities are primary contributors to the eutrophication in coastal seas [*Hu et al.*, 2006; *Lee et al.*, 2009]. Meanwhile, dissolved organic matter and oxygen from the sea can facilitate the attenuation of land-sourced pollutants by aerobic degradation and other biochemical transformations [*Robinson et al.*, 2009; *Heiss et al.*, 2017]. The reaction rate of these processes is dependent on the input of different marine-based constituents, such as oxygen and dissolved organic matter [*Santos et al.*, 2008; *Charbonnier et al.*, 2013; *Anwar et al.*, 2014]. The thermally variable USP would produce a variable influx of these compounds to the subsurface and would potentially influence the amount of terrestrial chemicals discharged to the marine environment.

Several biochemical processes that occur in the USP have reaction rates dependent on intensity of the mixing between freshwater and groundwater and size of the upper mixing zone, e.g., nitrogen transformations, denitrification and respiration, etc. [*Robinson et al.*, 2009; *Anwar et al.*, 2014; *Heiss et al.*, 2017]. The removal of land-sourced nitrogen, in particular, is favored on the landward side of the upper mixing zone and is enhanced as the upper mixing zone expands from increased tidal amplitude, hydraulic conductivity or hydrodynamic dispersion [*Heiss et al.*, 2017]. The thermally induced expansion of the upper mixing zone could thus have important implications for the loading of nitrogen and other land-sourced nutrients to the ocean. Besides, the upper seawater circulation generated by tidal oscillation is now also a thermal zone. The temperature of this zone is regulated largely by seawater temperature. The heterogeneous thermal pattern is of particular importance to those biochemical reactions that are catalyzed by microorganisms whose reactivity, in many cases, is thermally dependent [*Holtan-Hartwig et al.*, 2002; *Veraart et al.*, 2011; *Charbonnier et al.*, 2013; *Zheng et al.*, 2016].

On the other hand, with regards to the understanding of the system processes, the freshwater-saltwater thermal imbalance adds to the complexity of coastal aquifer systems. The mean temperature contrast, as the main concern of this study, adds a background thermal heterogeneity to the domain, especially within the upper and lower saline regions. This thermal background introduces a second mechanism for inducing density gradients in addition to the salinity. The two types of density gradients can either amplify or dampen each other depending on the configuration of the temperature distribution. The simultaneous diffusion of heat and salt, hence, can produce different versions of double-diffusive convection, depending on the direction of the destabilizing vertical gradient [*Nield*, 1968; *Diersch and Kolditz*, 1998].

As the freshwater-seawater thermal contrast is widely different along global coastlines, the temperature effect on coastal aquifer hydrodynamics is largely locally specific. A variety of system properties, namely beach slope, permeability, heterogeneity, etc. should affect the manifestation of the temperature effect. Nevertheless, some primary observations can be drawn out based on the distribution of temperature contrast calculated from the data of *Locarnini et al.* [2013 and *Benz et al.* [2017] (supporting information Figure S4). Coastal aquifers near the warm temperate zones (north and south) might experience the most significant thermal effects as the seawater temperature diverges from the groundwater temperature, colder to the north and warmer to the south. The thermal setting could have important effect on the coastal dynamics at the cold temperate zone where the seawater is also much warmer than groundwater. Closer to the equator, the temperature difference reduces, hence, the thermal effect is less pronounced.

## 5. Conclusions

We have examined the effect of temperature on the flow, salinity distribution and circulating seawater flux in both laboratory- and field-scale unconfined aquifers subjected to tides. The results lead to the following conclusions:

(1) Salinity distributions in coastal aquifers vary in response to the aquifer-ocean temperature contrasts. As the seawater temperature increases, the USP expands while the lower saltwater wedge retreats seaward.

(2) The higher seawater temperature increases the hydraulic conductivity and enhances the aquifer-ocean mass exchange. In particular, the tidally-induced seawater circulation within the USP increases remarkably, resulting in increased submarine groundwater discharge.

(3) As the tidal amplitude increases, the USP expands, and the lower saltwater wedge retreats. Both the tide-induced seawater circulation and submarine groundwater discharge increase. These effects are intensified as the seawater temperature increases.

Real aquifers are expected to exhibit more complexity than considered here with regards to their thermal configuration including seasonality as well as daily variations of seawater temperature. Such transient conditions require more investigation. Nevertheless, by using fixed temperature differences, the present results provide the overall behavior of effects of temperature differences between coastal waters and aquifers. As the results show, differences in flow patterns and configuration of flow regions within coastal aquifers can be markedly affected by temperature contrasts between fresh groundwater and seawater.

## Acknowledgements

This work was supported by the National Natural Science Foundation of China (51579077) and the Australian Research Council Discovery Projects (DP180104156 and DP19010372). The authors thank Susanne Benz for the groundwater temperature data. The SUTRA-MS model can be downloaded from the USGS website (https://water.usgs.gov/nrp/gwsoftware/SutraMS/SutraMS.html). The experimental data and the global temperature distribution along the coastline are available in the CUAHSI Hydroshare database (https://www.hydroshare.org/resource/ae753b61e37243ea873844894f6f0107/).


## References


Abarca, E., J. Carrera, X. Sánchez-Vila, and M. Dentz (2007), Anisotropic dispersive Henry problem, *Adv. Water Resour.*, *30*(4), 913–926, doi:10.1016/j.advwatres.2006.08.005.

Abdoulhalik, A., and A. A. Ahmed (2018), Transience of seawater intrusion and retreat in response to incremental water-level variations, *Hydrol. Process.*, doi:10.1002/hyp.13214.

Anderson, M. P. (2005), Heat as a ground water tracer, *Ground Water*, *43*(6), 951–968, doi:10.1111/j.1745-6584.2005.00052.x.

Anwar, N., C. Robinson, and D. A. Barry (2014), Influence of tides and waves on the fate of nutrients in a nearshore aquifer: Numerical simulations, *Adv. Water Resour.*, *73*, 203–213, doi:10.1016/j.advwatres.2014.08.015.

Benz, S. A., P. Bayer, and P. Blum (2017), Global patterns of shallow groundwater temperatures, *Environ. Res. Lett.*, *12*(3), doi:10.1088/1748-9326/aa5fb0.

Carsel, R. F., and R. S. Parrish (1988), Developing joint probability descriptions of soil water retention, *Water Resour. Res.*, *24*(5), 755–769.

Chang, S. W., and T. P. Clement (2012), Experimental and numerical investigation of saltwater intrusion dynamics in flux-controlled groundwater systems, *Water Resour. Res.*, *48*(9), doi:10.1029/2012WR012134.

Charbonnier, C., P. Anschutz, D. Poirier, S. Bujan, and P. Lecroart (2013), Aerobic respiration in a high-energy sandy beach, *Mar. Chem.*, *155*, 10–21, doi:10.1016/j.marchem.2013.05.003.

Cooper, H. H., F. A. Kohout, H. R. Henry, and R. E. Glover (1964), *Sea water in coastal aquifers*.

Diersch, H.-J. G., and O. Kolditz (1998), Coupled groundwater flow and transport: 2. Thermohaline and 3D convection systems, *Adv. Water Resour.*, *21*(5), 401–425, doi:10.1016/S0309-1708(97)00003-1.

Diersch, H. J. G., and O. Kolditz (2002), Variable-density flow and transport in porous media: Approaches and challenges, *Adv. Water Resour.*, *25*(8–12), 899–944, doi:10.1016/S0309-1708(02)00063-5.

Van Genuchten, M. T. (1980), A closed-form equation for predicting the hydraulic conductivity of unsaturated soils, *Soil. Sci. Soc. Am.*, *44*(5), 892–898.

Goswami, R. R., and T. P. Clement (2007), Laboratory-scale investigation of saltwater intrusion dynamics, *Water Resour. Res.*, *43*(4), doi:10.1029/2006WR005151.

Heiss, J. W., and H. A. Michael (2014), Saltwater-freshwater mixing dynamics in a sandy beach aquifer over tidal, spring-neap, and seasonal cycles, *Water Resour. Res.*, *50*, 6747–6766, doi:10.1002/2014WR015574.

Heiss, J. W., V. E. A. Post, T. Laattoe, C. J. Russoniello, and H. A. Michael (2017), Physical controls on biogeochemical processes in intertidal zones of beach aquifers, *Water Resour. Res.*, *53*(11), 9225–9244, doi:10.1002/2017WR021110.

Holtan-Hartwig, L., P. Dörsch, and L. R. Bakken (2002), Low temperature control of soil denitrifying communities: Kinetics of N2O production and reduction, *Soil Biol. Biochem.*, *34*(11), 1797–1806, doi:10.1016/S0038-0717(02)00169-4.

Hu, C., F. E. Muller-Karger, and P. W. Swarzenski (2006), Hurricanes, submarine groundwater discharge, and Florida's red tides, *Geophys. Res. Lett.*, *33*(11), doi:10.1029/2005GL025449.

Hughes, B. J. D., and W. E. Sanford (2005), *SUTRA—MS a version of SUTRA modified to simulate heat and multiple-solute transport*.

Jamshidzadeh, Z., F. T.-C. Tsai, S. A. Mirbagheri, and H. Ghasemzadeh (2013), Fluid dispersion effects on density-driven thermohaline flow and transport in porous media, *Adv. Water Resour.*, *61*, 12–28, doi:10.1016/j.advwatres.2013.08.006.

Kim, K. H., J. W. Heiss, H. A. Michael, W. J. Cai, T. Laattoe, V. E. A. Post, and W. J. Ullman (2017), Spatial patterns of groundwater biogeochemical reactivity in an intertidal beach aquifer, *J. Geophys. Res. Biogeosciences*, *122*(10), 2548–2562, doi:10.1002/2017JG003943.

Kuan, W. K., G. Jin, P. Xin, C. Robinson, B. Gibbes, and L. Li (2012), Tidal influence on seawater intrusion in unconfined coastal aquifers, *Water Resour. Res.*, *48*(2), doi:10.1029/2011WR010678.

Lee, K. S. (2012), *Green Energy and Technology*.

Lee, Y. W., D. W. Hwang, G. Kim, W. C. Lee, and H. T. Oh (2009), Nutrient inputs from submarine groundwater discharge (SGD) in Masan Bay, an embayment surrounded by heavily industrialized cities, Korea, *Sci. Total Environ.*, *407*(9), 3181–3188, doi:10.1016/j.scitotenv.2008.04.013.

Li, L. Barry, D. A. (1999), SGD and associated chemical input to a coastal sea, *Water Ressources Res.*, *35*, 3253–3259.

Locarnini, R. A. et al. (2013), World Ocean Atlas 2013, Volume 2: Temperature, *NOAA Atlas NESDIS*, *1*(73), 40. Available from: https://www.nodc.noaa.gov/cgi-bin/OC5/woa13/woa13.pl.

Van Lopik, J. H., N. Hartog, W. J. Zaadnoordijk, D. G. Cirkel, A. Raoof, J. H. Van Lopik, N. Hartog, W. Jan, and D. G. Cirkel (2015), Salinization in a stratified aquifer induced by heat transfer from well casings, *Adv. Water Resour.*, *86*, 32–45, doi:10.1016/j.advwatres.2015.09.025.

Lu, C., P. Xin, J. Kong, L. Li, and J. Luo (2016), Analytical solutions of seawater intrusion in sloping confined and unconfined coastal aquifers, *Water Resour. Res.*, *52*(9), 6989–7004, doi:10.1002/2016WR019101.

Moore, W. S. (2010), The effect of submarine groundwater discharge on the ocean, *Ann. Rev. Mar. Sci.*, *2*(1), 59–88, doi:10.1146/annurev-marine-120308-081019.

Nield, D. A. (1968), Onset of thermohaline convection in a porous medium, *Water Ressources Res.*, *4*(3).

Pagnutti, M., R. E. Ryan, G. Cazenavette, M. Gold, R. Harlan, E. Leggett, and J. Pagnutti (2017), Laying the foundation to use Raspberry Pi 3 V2 camera module imagery for scientific and engineering purposes, *J. Electron. Imaging*, *26*(1), 013014, doi:10.1117/1.JEI.26.1.013014.

Robinson, C., L. Li, and D. A. Barry (2007), Effect of tidal forcing on a subterranean estuary, *Adv. Water Resour.*, *30*, 851–865, doi:10.1016/j.advwatres.2006.07.006.

Robinson, C., A. Brovelli, D. A. Barry, and L. Li (2009), Tidal influence on BTEX biodegradation in sandy coastal aquifers, *Adv. Water Resour.*, *32*(1), 16–28, doi:10.1016/j.advwatres.2008.09.008.

Robinson, C. E., P. Xin, I. R. Santos, M. A. Charette, L. Li, and D. A. Barry (2018), Groundwater dynamics in subterranean estuaries of coastal unconfined aquifers: Controls on submarine groundwater discharge and chemical inputs to the ocean, *Adv. Water Resour.*, *115*, 315–331, doi:10.1016/j.advwatres.2017.10.041.

Rubeis, T. De, I. Nardi, and M. Muttillo (2017), Development of a low-cost temperature data monitoring. An upgrade for hot box apparatus, *J. Phys. Conf. Ser.*, *923*(1), doi:10.1088/1742-6596/923/1/012039.

Santos, I. R., W. C. Burnett, J. Chanton, B. Mwashote, I. G. N. A. Suryaputra, and T. Dittmar (2008), Nutrient biogeochemistry in a Gulf of Mexico subterranean estuary and groundwater-derived fluxes to the coastal ocean, *Limnol. Oceanogr.*, *53*(2), 705–718, doi:10.4319/lo.2008.53.2.0705.

Shen, C., C. Zhang, G. Jin, J. Kong, and L. Li (2016), Effects of unstable flow on solute transport in the marsh soil and exchange with coastal water, *Geophys. Res. Lett.*, *43*(23), 12,091-12,101, doi:10.1002/2016GL070576.

Slomp, C. P., and P. Van Cappellen (2004), Nutrient inputs to the coastal ocean through submarine groundwater discharge: Controls and potential impact, *J. Hydrol.*, *295*(1–4), 64–86, doi:10.1016/j.jhydrol.2004.02.018.

Smith, A. J. (2004), Mixed convection and density-dependent seawater circulation in coastal aquifers, *Water Resour. Res.*, *40*(8), doi:10.1029/2003WR002977.

Taniguchi, M. (1993), Evaluation of vertical groundwater fluxes and thermal properties of aquifers based on transient temperature-depth profiles, , *29*(7), 2021–2026.

Veraart, A. J., J. J. M. de Klein, and M. Scheffer (2011), Warming can boost denitrification disproportionately due to altered oxygen dynamics, *PLoS One*, *6*(3), 2–7, doi:10.1371/journal.pone.0018508.

Voss, C. I., and A. M. Provost (2010), SUTRA: A model for saturated-unsaturated, variable-density ground-water flow with solute or energy transport, *Water-Resources Investig. Rep. 02-4231*, 300 p.

Werner, A. D., M. Bakker, V. E. A. Post, A. Vandenbohede, C. Lu, B. Ataie-Ashtiani, C. T. Simmons, and D. A. Barry (2013), Seawater intrusion processes, investigation and management: Recent advances and future challenges, *Adv. Water Resour.*, *51,* 3–26, doi:10.1016/j.advwatres.2012.03.004.

Xin, P., C. Robinson, L. Li, D. A. Barry, and R. Bakhtyar (2010), Effect of wave forcing on a subterranean estuary, *Water Resour. Res.*, *46*(1), 17, doi:10.1016/j.advwatres.2006.07.006.

Xin, P., S. S. J. Wang, C. Robinson, L. Li, Y.-G. Wang, and D. A. Barry (2014), Memory of past random wave conditions in submarine groundwater discharge, *Geophys. Res. Lett.*, *41*(7), 2401–2410, doi:10.1002/2014GL059617.

Xin, P., S. S. J. Wang, C. Shen, Z. Zhang, C. Lu, and L. Li (2018), Predictability and quantification of complex groundwater table dynamics driven by irregular surface water fluctuations, *Water Resour. Res.*, *54,* doi:10.1002/2017WR021761.

Yu, X., P. Xin, C. Lu, C. Robinson, L. Li, and D. A. Barry (2017), Effects of episodic rainfall on a subterranean estuary, *Water Resour. Res.*, *53*(7), 5774–5787, doi:10.1002/2017WR020809.

Yu, X., P. Xin, S. S. J. Wang, C. Shen, and L. Li (2019a), Effects of multi-constituent tides on a subterranean estuary, *Adv. Water Resour.*, *124*, 53–67, doi:10.1016/j.advwatres.2018.12.006.

Yu, X., P. Xin, and C. Lu (2019b), Seawater intrusion and retreat in tidally-affected unconfined aquifers: Laboratory experiments and numerical simulations, *Adv. Water Resour.*, *132*, 103393, doi:10.1016/j.advwatres.2019.103393.

Zhang, C., D. William, and X. Lei (2017), Design, manufacture and calibration of sensors for monitoring tailings settling, consolidation and desiccation, in *Proceedings of the 2017 Tailings and Mine Waste, Banff, Canada*, pp. 206–304, Banff, Alberta, Canada.

Zhang, C., D. William, J. Lei, Y. Zhu, and M. O'Neil (2018), Instrumented column testing of salt uptake from compacted red mud into a cover., in *Proceeding of the Mine Waste and Tailings Conference 2018*, Brisbane, Australia.

Zheng, L., M. B. Cardenas, and L. Wang (2016), Temperature effects on nitrogen cycling and nitrate removal-production efficiency in bed form-induced hyporheic zones, *J. Geophys. Res. Biogeosciences*, *121*(4), 1086–1103, doi:10.1002/2015JG003162.